https://doi.org/10.1016/j.nanoen.2018.08.010

Ni/Co-Based Nanosheet Arrays for Efficient Oxygen Evolution Reaction

Yong Li[a,1], Liangsheng Hu[a,1], Weiran Zheng[a], Xiang Peng[b], Mengjie Liu[a], Paul K. Chu[b,*], and Lawrence Yoon Suk Lee[a,*]

[a] Department of Applied Biology and Chemical Technology, The Hong Kong Polytechnic University, Hung Hom, Kowloon, Hong Kong SAR, China

[b] Department of Physics and Department of Materials Science and Engineering, City University of Hong Kong, Tat Chee Avenue, Kowloon, Hong Kong SAR, China

[*]Corresponding authors:

E-mail: lawrence.ys.lee@polyu.edu.hk (L. Y. S. Lee); paul.chu@cityu.edu.hk (P. K. Chu)

[1]These authors contributed equally to this work

Abstract

Efficient oxygen evolution reaction (OER) catalysts composed of earth-abundant elements are crucial to the development of practical and environmentally friendly water splitting systems. Herein, composite $NiCoO_2$/CoO/Ni_3N nanosheet arrays (NiCoON NSAs/NF) are fabricated *in situ* on the 3D nickel foam. In the alkaline solution, the NiCoON nanocomposites have excellent catalytic OER properties, such as a small overpotential of 247 mV (at 10 mA cm^{-2}) and Tafel slope of 35 mV dec^{-1}, which are better than those of $Ni_xCo_{3-x}O_4$ and most Ni- and Co-based catalysts. There are more active sites with oxygen vacancies on NiCoON NSAs after the treatment with NH_3 and the face-centered cubic $NiCoO_2$ enhances the formation of active Ni-Co layered hydroxide/oxyhydroxide species (NiOOH) in comparison with spinal-typed $Ni_xCo_{3-x}O_4$ during the electrochemical process. In addtion, the Ni^{3+}-rich surface together with Co incorporation facilitates the formation of β-NiOOH. Our study reveals that control of active species on NiCoON NSAs/NF leads to high activity and stability in OER catalysis.

Keywords: oxygen evolution reaction; electrocatalysis; NiCo nanocomposite; nanosheet array

1 Introduction

Global concern on the shortage of fossil fuels has triggered extensive research on alternative energy sources and storage and hydrogen is one of the most suitable substitutes for fossil fuels due to the high energy density and zero pollutant emission. However, about 90% of hydrogen is currently being produced *via* hydrocarbon reforming which is neither energy efficient nor environmental friendly. As an alternative for clean and efficient hydrogen production and storage, electrochemical water splitting ($2H_2O \rightarrow O_2 + 2H_2$) has spurred extensive studies in recent years [1,2]. However, the process usually suffers from the low efficiency and high overpotential due to the sluggish kinetics of the anodic oxygen evolution reaction (OER) which involves O−H bond breaking, energy demanding O-O bond formation, and multiple electron transfer steps [3]. To accelerate the kinetics and reduce the overpotential in OER, much effort has been made to develop an efficient electrocatalyst by considering both the morphologic and electronic aspects [4–6]. Among the various electrocatalytic materials developed so far, Ru- and/or Ir-based catalysts deliver the best OER performance but still require an overpotential of 250~300 mV to obtain a current density $\geq$ 10 mA cm^{-2} [7,8]. Moreover, the high cost and scarcity of noble metals hamper more widespread application and hence, more earth-abundant transition metals such as, Ni, Co, Fe, and Mn have been suggested as alternative electrocatalysts in OER [9–13]. In particular, nickel-based catalysts have recently been demonstrated to deliver comparable or even superior OER performance [14–16].

The NiOOH-type structure constitutes an active OER catalyst under alkaline conditions [17–19] and Ni-based solid-state catalysts such as metals [20], oxides [21], oxyhydroxides [22], phosphides [19], nitrides [23], sulfides [15], selenides [24,25], borates [26,27], and borides [28–30] have been shown to undergo the oxidation reaction of $Ni^{2+} \rightarrow Ni^{3+}$ creating disordered NiOOH centers [31]. These oxyhydroxides act as active sites for O_2 generation as the highly oxidized metal cations can facilitate the formation of oxyhydroxide species which is the key

intermediate in OER process [32]. Catalysts with mixed transition metals have been shown to have better catalytic activity than a single-metal system. Trotochaud *et al*. [33] reported that incorporation of iron into $Ni(OH)_2$/NiOOH thin films lowered the overpotential of pure NiOOH and binary Ni-Co oxide / NiCo alloy with oxide (CoO-NiO-NiCo) exhibited better catalytic activity in OER than the individual Ni- or Co-based catalysts [34,35]. It is believed that the addition of Fe or Co oxides into the Ni-based catalysts enriches the Ni^{3+} population on the surface to facilitate the formation of NiOOH and adorption of OH^- in an alkaline solution [22].

In addition to the active catalytic sites, electroconductivity is another key factor determining the performance of electrocatalysts [23,36]. The commonly employed strategies to improve the conductivity of metal oxides are: (1) combining oxides with highly conductive materials such as carbon nanotubes, graphene, metallic carbides, and nitrides [37–39] and (2) introducing oxygen vacancies or heteroatom dopants into metal oxides. The latter has been reported to not only augment the conductivity and charge mobility, but also facilitate polaron hopping between adjacent catalytic sites [40–42]. Particularly, nitrogen doping is an efficient way to improve the conductivity by creating a nitrogen-rich surface boasting excellent adsorption of oxygen species and OER performance [43,44].

Although Co incorporation into Ni-based systems has been studied [18,27,38–42], the role of Co in OER catalysis is still controversial and not clearly understood. For instance, Boettcher *et al.* [48] reported that Co incorporation into NiO lowered the OER performance. The NiO with a rock-salt structure was claimed to be more easily converted *in situ* to the layered hydroxide/oxyhydroxide phase, whereas the spinel-type structure resulting from Co insertion might inhibit this transformation. On the contrary, Tour *et al*. [34] reported that nanoporous Ni-rich (10 atom % Co) Ni–Co binary oxides had an enlarged active surface area and reduced charge transfer resistance, which enhanced the catalytic activity in OER in comparison with pure Ni or Co oxide films. Besides, hybrid NiO/Co_3O_4 nanoparticles prepared on nitrogen-

doped carbon (NiO/Co_3O_4@NC) were shown to have better activity than NiO@NC because of the intimate interaction between Ni and Co through O bridge (Co-O-Ni) at the interface of NiO and Co_3O_4 [49].

Herein, we present a systematic study on the Co and N doping effects on the structure and electrocatalytic properties of nickel oxide by controlling the Ni:Co ratio and annealing conditions. A porous $NiCoO_2/CoO/Ni_3N$ nanosheet array (abbreviated as NiCoON NSAs) prepared on the 3-dimensional (3D) nickel foam (NiCoON NSAs/NF) is demonstrated to be an active and stable electrocatalyst for OER as manifested by an overpotential of 247 mV at 10 mA cm^{-2} and Tafel slope of 35 mV dec^{-1}, which are better than those of Ir-based electrocatalysts [48]. Our results reveal the origin of the electrocatalytic activity of the OER catalyst and insights in the design of catalysts based on Ni and other transition metals.

2 Experimental details

2.1 Synthesis of $Ni_xCo_{3-x}O_4$ NSAs/NF and NiCoON NSAs/NF

The synthesis method was adopted from the reported procedues with slight modifications [50]. In the preparation of $Ni_xCo_{3-x}O_4$ NSAs, different ratios of the starting $Ni(NO_3)_2 \cdot 6H_2O$ to $Co(NO_3)_2 \cdot 6H_2O$ precursor were mixed with the total concentration kept at 3.93 mmol. 26.25 mmol urea and 10.5 mmol NH_4F were added to 70 mL of water and stirred for 1 h at room temperature before transferring to a 100 mL Teflon-lined stainless-steel autoclave. The nickel foam (2 × 3 cm^2) was used as the substrate. The autoclave was heated to 100 °C for 8 h to obtain the cobalt-nickel hydroxide precursor. After annealing of the precursor at 350 °C in air for 1 h, $Ni_xCo_{3-x}O_4$/NF with different Ni:Co ratios (*n*:*m*) were obtained. In the preparation of NiCoON(*n*:*m*) NSAs/NF, the nickel hydroxide precursor was heated to 300-400 °C under flowing ammonia (NH_3, 35 sccm) for 3 h followed by cooling in flowing Ar.

2.2 Structural characterization

The morphology and structure of the samples were characterized by field-emission scanning electron microscopy (FE-SEM, JEOL), transmission electron microscopy (TEM, JEOL-2100F equipped with an X-ray energy dispersive spectrometer (EDX)), X-ray diffraction (XRD, X' Pert PRO PHILIPS with Cu Ka radiation), and Raman scattering spectroscopy. The chemical states were determined by X-ray photoelectron spectroscopy (XPS, AC-2, Riken Keiki).

2.3 Electrochemical characterization

A three-electrode system was adopted in the electrochemical measurement conducted on an electrochemical workstation (CHI760E, Chenhua Shanghai) at room temperature. The nanosheet arrays on the nickel foam (3×5 mm^2) served as the working electrode (catalyst loading = *ca*. 0.6 mg cm^{-2}) and Pt flake and saturated calomel electrode (SCE) were the counter and reference electrodes, respectively. The working electrode was activated by cycling between 0 and 0.6 V (*vs*. SCE) for ten cycles at a scanning rate of 10 $mV \cdot s^{-1}$ before performing linear sweep voltammetry (LSV). The catalytic OER was evaluated by LSV at a scanning rate of 5 $mV \cdot s^{-1}$ between 1.0 and 1.6 V (*vs*. reversible hydrogen electrode, RHE). Electrochemical impedance spectroscopy (EIS) was carried in the frequency range between 100 kHz and 0.01 Hz at 0.55 V (*vs*. SCE). The polarization curves were iR-compensated according to the equation ($V_{calibration} = V_{original} - iR_{solution\ resistance}$, where the solution ohmic drop ($R_{solution\ resistance}$) was measured from the EIS Nyquist plot). The current-time (*i*-t) curve and LSV were obtained to assess the stability of the nanosheet arrays and all the electrochemical measurements were performed in 1.0 M KOH.

2.4 Reversible hydrogen electrode calibration

The SCE was calibrated to the RHE with Pt electrodes as both the working and counter electrodes. Using a SCE as the reference electrode, cyclic voltammograms (CVs) were recorded from -1.1 to -0.9 V (*vs*. SCE) in a high-purity hydrogen saturated electrolyte at a scanning rate of 5 mV s^{-1} and the CV plots are shown in **Fig. S1**.

3 Results and discussion

3.1 Morphology

The NiCoON(1:2) NSAs (Ni:Co ratio = 1:2) are fabricated *in situ* on a 3D nickel foam (NF) *via* a hydrothermal reaction followed by annealing in ammonia (**Scheme 1**). **Fig. 1a** and the inset depict the low and high-magnification SEM images of NiCoON(1:2) NSAs/NF revealing that dense and uniform nanosheets are formed on the Ni foam surface. The morphology of NiCoON(1:2) NSAs/NF is similar to that of $NiCo_2O_4$ NSAs/NF (**Fig. S2**) prepared as a control by annealing the hydrothermal product in air.

3.2 Crystal structure

Fig. 1b shows the XRD pattern of NiCoON(1:2) NSAs/NF and the diffraction peaks can be indexed to rock-salt $NiCoO_2$ (JCPDS 10-0188), CoO (JCPDS 48-1719), and Ni_3N (JCPDS 10-0280), except the strong Ni peaks arising from the substrate. The TEM image in **Fig. 1c** discloses a rough surface on the NiCoON(1:2) nanosheet, suggesting the reduction and partial replacement of O with N during annealing and the formation of mesopores with a large surface area.

The high-resolution TEM (HR-TEM) image (**Fig. 1d**) reveals three distinct species with interplanar distances of 0.244, 0.214, and 0.246 nm attributed to the (111) plane of rock-salt $NiCoO_2$, (002) plane of hexagonal Ni_3N, and (111) plane of cubic CoO, respectively, confirming the co-existence of $NiCoO_2$, CoO, and Ni_3N. The elemental mappings obtained by

EDS in **Fig. S3** show that Ni, Co, O, and N are uniformly distributed in the NiCoON(1:2) nanosheet. The composition and chemical states of the $NiCo_2O_4$ and NiCoON(1:2) NSAs are determined by XPS, and the spectra and fitted results are presented in **Figs. 1e**, **1f**, and **S4**. Although the two fitted peaks for Ni $2p_{3/2}$ (**Fig. 1e**) indicate the presence of Ni^{3+} (855.5 eV) and Ni^{2+} (853.9 eV) in the $NiCo_2O_4$ and NiCoON(1:2) NSAs [22], the calculated Ni^{3+}/Ni^{2+} ratio of NiCoON(1:2) (14.2) is larger than that of $NiCo_2O_4$ (4.8), indicating that the NiCoON(1:2) NSAs has a Ni^{3+}-rich surface. Moreover, the Ni_3N peak at 852.4 eV is detected only from the NiCoON(1:2) NSAs [23], providing evidence of partial reduction of Ni^{2+} to Ni^{1+} by ammonia. The N 1s spectrum confirms the presence of Ni_3N species on the NiCoON(1:2) NSAs surface (**Fig. S4a**). The O 1s spectra acquired from both samples exhibit three characteristic peaks corresponding to the oxygen-metal bond (530.1 eV; O1), surface oxygen defect/vacancy species (531.5 eV; O2), and hydroxyl groups or surface-adsorbed oxygen (532.3 eV; O3, **Fig. 1f**) [51,52]. Comparison of the O2 peaks indicates that the NiCoON(1:2) NSAs contains more oxygen vacancies than the $NiCo_2O_4$ NSAs. Two Co oxidation states are identified from the $NiCo_2O_4$ and NiCoON(1:2) NSAs with the two Co $2p_{3/2}$ peaks at 780.9 and 779.5 eV corresponding to Co^{2+} and Co^{3+}, respectively (**Fig. S4b**) [51,53]. The calculated Co^{2+}/Co^{3+} ratio of NiCoON(1:2) (9.1) is larger than that of $NiCo_2O_4$ (1.6) due to the reducing conditions in the NiCoON(1:2) NSAs synthesis which preferentially favors the formation of species with a smaller valance. Compared with the structure of $NiCo_2O_4$ which has the general formula of $Co^{2+}{}_{1-x}Co^{3+}{}_x$ $[Co^{3+}Ni^{2+}{}_xNi^{3+}{}_{1-x}]O_4$ ($0 \leq x \leq 1$) [54], the structure of the precursor is believed to be partially destroyed during ammonia annealing and Ni^{2+} is further reduced to Ni^{+} as consistent with the XRD and TEM results.

3.3 Electrochemical performance

To evaluate the electrocatalytic OER characteristics of NiCoON(1:2) NSAs/NF, linear sweep voltammetry (LSV) and chronopotentiometry are performed and compared with the

results obtained from the two control samples, $NiCo_2O_4$ NSAs/NF and NF. **Fig. 2a** compares the LSV curves obtained at a scanning rate of 5 mV s^{-1}. The pre-OER oxidation peak at a potential range of 1.26 to 1.37 V (*vs*. RHE unless stated otherwise) of all the samples is related to the oxidation of Ni^{2+} to Ni^{3+} [23,55]. At higher potentials, NiCoON(1:2) NSAs/NF shows the smallest OER onset potential with a larger specific current density (j). An overpotential (η) of 247 mV is measured to reach a current density of 10 mA cm^{-2} and it is less than those of $NiCo_2O_4$ NSAs/NF (284 mV) and NF (351 mV). The corresponding Tafel plots (η *vs.* log (j), **Fig. 2b**) impart more details about the kinetics. NiCoON(1:2) NSAs/NF has the smallest Tafel slope (35 mV dec^{-1}) than others (45 mV dec^{-1} for $NiCo_2O_4$ NSAs/NF and 75 mV dec^{-1} for NF) and the overpotential and Tafel slope of NiCoON(1:2) NSAs/NF are among the best compared with other Ni-based electrocatalysts in the literature (**Table S1**). To investigate the factors leading to the catalytic enhancement, electrochemical impedance spectroscopy (EIS) is carried out. **Fig. 2c** compares the Nyquist plots acquired from the NF, $NiCo_2O_4$ NSAs/NF, and NiCoON(1:2) NSAs/NF. The smallest semi-circle observed from NiCoON(1:2) NSAs/NF indicates the smallest charge transfer resistance (R_{ct}, 4.7 Ω) at 1.58 V. Compared with NF and $NiCo_2O_4$ NSAs/NF, the solution resistance (R_s) of NiCoON(1:2) NSAs/NF is slightly increased due to the increased surface roughness [56]. The areal capacitance of NiCoON(1:2) NSAs/NF (141 mF cm^{-2}) exceeds those of $NiCo_2O_4$ NSAs/NF and NF by 150 % and 1,800 %. The larger active surface area contributes to the OER rate (**Fig. S5**) and NiCoON(1:2) NSAs/NF also exhibits an excellent long-term electrochemical stability. To investigate the corrosion behavior and durability of samples, different current densities (10, 35, and 55 mA cm^{-2}) were applied to the NiCoON NSAs/NF with a longer time (30 h) reaction. As shown in **Fig. 2d**, the sample is stable even after 30 h reaction at high current densities. The polarization curve also does not show any significant loss in the current density or increase in the overpotential after continuous 1,000 potential cycles (inset in **Fig. 2d**). To evaluate the catalytic efficiency of NiCoON(1:2) NSAs/NF, the amount of oxygen produced during the OER electrolysis at 14 mA cm^{-2} was

measured for 90 min and compared with the theoretical values (**Fig. S6**). The result yields a high faradaic efficiency of 97.8 %, indicating that almost all charges are associated with the OER without any other electron pathway or side reaction.

3.3.1 Active sites

The active sites on the transition metal (Ni, Fe, Co)-based OER catalysts in alkaline media have been identified to be oxyhydroxides (M-OOH) [10]. With regard to the Ni-based catalysts, OER is proposed to proceed in four steps [23]. In brief, surface Ni atoms are first oxidized to NiOOH with sequential oxidation to $NiO(OH)_2$ and $NiOO_2$ at higher potentials. Further increase in the potential generates O_2 on $NiOO_2$ and regenerates NiOOH species. Usually, formation of NiOOH, $NiO(OH)_2$, and $NiOO_2$ is considered as the OER rate determining steps. To gain insights into the relationship between the material structure and OER activity, the changes on the catalyst surface are monitored by HR-TEM, XPS, and Raman scattering.

Fig. 3a displays the HR-TEM image of the post-OER NiCoON(1:2) in which a 15-20 nm thick amorphous layer is evident along the edge. XPS indicates that the surface layer is composed of oxide and oxyhydroxide species. The two peaks in the Ni $2p_{3/2}$ spectrum (**Fig. 3b**) correspond to $Ni(OH)_2$ (856.0 eV) and NiOOH (857.1 eV) [57] and those in the O 1s spectrum are assigned to oxygen-metal bonds (530.1 eV; O1), $Ni(OH)_2$ (531.4 eV), NiOOH (532.0 eV), absorbed oxygen (532.6 eV), and H_2O (533.9 eV) [52]. The NiOOH species on the surface of post-OER NiCoON(1:2) NSAs/NF is verified by the Raman spectra in **Fig. 3c**. After OER, the $NiCoO_2$ peak at 532 cm^{-1} split into two peaks at 474 and 554 cm^{-1} corresponding to NiOOH [32,58]. It is clear from the post-OER characterization that the electrocatalytically active species is *in situ* formed on the NiCoON(1:2) NSAs/NF surface during OER. It is noted that active species (NiOOH) is produced less on the post-OER $NiCo_2O_4$ NSAs/NF as revealed by HR-TEM and Raman scattering (**Fig. S7**). On the other hand, the Co^{2+}/Co^{3+} ratio in the post-

OER NiCoON(1:2), calculated from XPS data, has decreased to 1.4 (**Fig. S8**). This ratio is close to that of Co_3O_4 (1.2) [59] or $NiCo_2O_4$ (1.6), both of which have a spinel structure.

3.3.2 Effects of annealing temperature

The annealing temperature is an important factor affecting the amount of N dopant in the materials and the degree of reduction. By adjusting the annealing temperature between 300 and 400 °C under ammonia, the composition of the product can be controlled as shown by the XRD data in **Fig. 4a**. The XRD patterns of the samples annealed at 300, 350, 380, and 400 °C can be indexed to spinel $NiCo_2O_4$, $NiCoO_2$/CoO/Ni_3N composite (NiCoON(1:2)), (Ni, $Co)_3N$, and NiCo alloy, respectively. The SEM and TEM images of the (Ni, $Co)_3N$ and NiCo alloy NSAs/NF annealed at higher temperatures disclose the porous structures with large surface areas (**Fig. S9**) and higher conductivity. In the electrocatalytic OER tests shown in **Fig. 4b**, the sample annealed at 350 °C (NiCoON(1:2)) outperforms the other NiCo bimetallic catalysts indicating that $NiCoO_2$/CoO/Ni_3N enhances OER catalysis with the aid of the abundant active sites on the surface. It is also noted that the NiCoON(1:2) exhibits higher background current than the others due to large pseudocapacitive current contribution from $NiCoO_2$ and CoO, both of which are good capacitor candidates. The sample annealed at 300 °C shows OER characteristics similar to those of spinel $NiCo_2O_4$ treated at 350 °C in air due to the similar surface composition and structure.

3.3.3 Effects of Ni to Co ratio

The Ni to Co ratio in the NiCo-based catalysts determines the morphology and catalytic OER properties [34]. To investigate the influence of Co incorporation, a series of NiCo precursors with predetermined Ni:Co ratios are prepared and annealed at 350 °C in ammonia. Formation of uniform nanosheets on the NF is confirmed with the samples of various Ni:Co ratios (**Fig. S10**). When only Ni was used without Co, Ni_3N/NF nanosheets of a smaller coral

moss-like structure resulted, owing to the fragile nature of Ni-O bond that easily breaks down and combines with N to yield Ni_3N. Meanwhile, when only Co was used for synthesis, pure CoO/NF was formed with an averge nanosheet size of 9.4 μm. As the Ni:Co ratio is changed from 1:3 to 3:1, the average size of the nanosheets decreases from 6.4 to 2.3 μm. The OER performance of the different morphologies are examined and the results are summarized in **Figs. 5a** and **5b**.

Pre-OER peaks corresponding to M^{2+} (M-OH; M = Ni, Co) to M^{3+} (M-OOH) oxidation are observed in the range of 1.25 to 1.45 V (inset in **Fig. 5a**) from all the samples [32,48,55]. As discussed before, the pre-OER peak is closely related to the OER activity. The current intensity or more precisely, the integrated peak area, of the pre-OER peak indicates the amount of active species (M-OOH) on the surface and consequently correlates with the OER efficiency of the catalyst. There is a strong dependence of the pre-OER peak potential on the sample composition. The pre-OER peak of the samples prepared with pure Ni or Co appears at around 1.4 V and shifts to a lower potential when the sample is prepared from the Ni/Co mixture. The pre-OER peak potential versus the ratio shows an inverted volcano shape (inset in **Fig. 5a**) and the sample with a Ni:Co ratio of 1:2 shows the smallest potential. A similar trend is observed from the overpotentials and Tafel slopes (**Fig. 5b**). The charge transfer resistance plot versus Ni:Co ratio follows the same trend (**Fig. S11**), suggesting that the 1:2 ratio of Ni:Co leads to the formation of the optimal NiCoON NSAs/NF composite with the lowest overpotential of 247 mV, the fastest reaction rate of 35 mA dec^{-1}, and the smallest resistance of 4.7 Ω.

To obtain better understanding of the OER characteristics, Raman scattering spectra are acquired from the post-OER different ratio of Ni to Co samples and compared in **Fig. 5c**. While only a small amount of active species, CoOOH, is detected from the pure Co-based electrode (Raman peak at 505 cm^{-1}), a large amount of another active species, NiOOH, is observed from the pure Ni- and Ni/Co mixture-based catalysts. The pair of dominant peaks at 474 and 554

cm^{-1} observed from all the Ni-containing samples are ascribed to Ni–O vibration in γ-NiOOH and β-NiOOH, respectively [32,55,60]. Bell's group [32] attributed the excellent OER activity of $Ni(OH)_2$ to the phase transformation of α-$Ni(OH)_2$ to β-$Ni(OH)_2$ phase. They also reported that β-NiOOH phase has an optimal adsorption energy for atomic oxygen close to that of IrO_2, concluding that the β-NiOOH phase is more active in catalyzing OER than the γ-NiOOH phase. However, further studies pointed out that the enhanced OER activity of β-NiOOH phase might arise from the Fe impurities (< 1 ppm) in the unpurified KOH electrolyte [61,62]. To rule out this impurity effect, we checked the Fe concentration in our electrolyte by ICP-OES, and only 0.035 ppm Fe was detected. Even with further purified electrolyte (0.004 ppm Fe), no significant difference in the OER activity was noticed with our samples (**Fig. S12**), implying that the Fe impurity is not affecting our experiments. Interestingly, the relative intensity of the β- and γ-NiOOH peaks varies with the Ni:Co ratio. Similar to the OER activity and Tafel slope (**Fig. 5b**), the γ-NiOOH to β-NiOOH peak ratio follows the inverted volcano-like trend as the Ni:Co ratio (**Fig. 5d**), suggesting the Ni:Co ratio plays a critical role in the formation of active sites. Ni and Co apparently facilitate the formation of the active NiOOH phase by modulating the electronic structure to rock-salt $NiCoO_2$ [48]. The amount of β-NiOOH increases gradually with the Co content and shows the maximum value at a Ni:Co ratio of 1:2. Incorporation of Co facilitates the structural transformation of surface Ni atoms from α-$Ni(OH)_2$ to β-$Ni(OH)_2$ [63], which are the pre-oxidation species of α-$Ni(OH)_2$ and β-$Ni(OH)_2$, respectively [32]. However, an excess amount of Co depletes Ni atoms from the surface and mitigates formation of active species. Our results are consistent with previous reports that the OER activity of Ni-based hydroxide is higher than that of Co-based hydroxide due to the weaker Ni–OH_{ad} (adsorbed OH species) interaction than Co–OH_{ad} interaction [9].

The superior OER performance observed from NiCoON NSAs/NF (Ni:Co = 1:2) can be explained from the following perspectives. Firstly, the rock-salt type $NiCoO_2$ can be eaily *in*

situ converted to the layered NiOOH as active catalytic sites for OER and Co enhances the formation of β-NiOOH giving rise to a Ni^{3+}-rich surface [22]. Secondly, the large amount of oxygen vacancies in NiCoON(1:2) NSAs/NF not only improves the charge mobility, but also lowers the adsorption energy of H_2O to further promote OER electrolysis [51,53]. Thirdly, Ni_3N in NiCoON(1:2) NSAs/NF improves the conductivity. The higher surface Fermi energy of Ni_3N, which is higher than that of oxide, allows the electron injection into NiOOH to reduce the overpotential [49,64]. Fourthly, direct growth of NiCoON(1:2) NSAs on the conductive NF provides an excellent pathway for collection and rapid transfer of electrons.

4 Conclusion

A series of NiCo-based nanosheet arrays prepared using different Ni:Co ratios on nickel foam contain various Ni/Co composites on the surface including oxides (spinel type $NiCo_2O_4$ and rock-salt type $NiCoO_2$), nitrides, and alloy are evaluated as OER electrocatalysts. The oxide/nitride NiCo-based nanosheet arrays exhibit an inverted volcano-like trend in the overpotentials and Tafel slopes for OER when the Co content is increased. Systematic comparisons of the catalytic activity, morphology, and composition reveal that the $NiCoO_2$/CoO/Ni_3N (NiCoON(1:2)) hybrid structure is a highly efficient OER catalyst and the controlled insertion of Co is crucial to the formation of β-NiOOH active species. The NiCoON(1:2) NSAs delivers the best OER performance such as a small overpotential (247 mV at 10 mA cm^{-2}) and Tafel slope (35 mV dec^{-1}), which outperforms those of Ir-based benchmark catalysts reported in the literature. Our results provide direct demonstration and guidelines on how to design and tune the structure and composition of electrocatalysts to obtain the optimal catalytic OER characteristics.

Acknowledgements

The authors thank the financial support from the Innovation and Technology Commission of Hong Kong and Hong Kong Polytechnic University. The TEM experiments were conducted at the Hong Kong Polytechnic University Research Facility in the Materials Characterization and Device Fabrication (UMF)-center for Electron Microscopy. We acknowledge the use of the facilities and engineering support by Dr. Wei Lu.

Appendix A. Supporting information

Supplementary data including SEM images, XRD patterns, Raman spectra, XPS results, and electrochemical plots associated with this article can be found in the online version at doi:

References

[1] M. Grätzel, Photoelectrochemical cells, Nature 414 (2001) 338–344.

[2] J.R. Swierk, T.E. Mallouk, Design and development of photoanodes for water-splitting dye-sensitized photoelectrochemical cells, Chem. Soc. Rev. 42 (2013) 2357–2387.

[3] J. Suntivich, K.J. May, H. A.Gasteiger, J.B. Goodenough, Y. Shao-Horn, A perovskite oxide optimized for oxygen evolution catalysis from molecular orbital principles, Science 334 (2011) 1383–1385.

[4] B. Cui, H. Lin, J.-B. Li, X. Li, J. Yang, J. Tao, Core-ring structured $NiCo_2O_4$ nanoplatelets: Synthesis, characterization, and electrocatalytic applications, Adv. Funct. Mater. 18 (2008) 1440–1447.

[5] Y. Lee, J. Suntivich, K.J. May, E.E. Perry, Y. Shao-Horn, Synthesis and activities of rutile IrO_2 and RuO_2 nanoparticles for oxygen evolution in acid and alkaline solutions, J. Phys. Chem. Lett. 3 (2012) 399–404.

[6] X. Xiong, C. You, Z. Liu, A.M. Asiri, X. Sun, Co-doped CuO nanoarray: An efficient oxygen evolution reaction electrocatalyst with enhanced activity, ACS Sustain. Chem. Eng. 6 (2018) 2883–2887.

[7] Y. Pi, Q. Shao, P. Wang, F. Lv, S. Guo, J. Guo, X. Huang, Trimetallic oxyhydroxide coralloids for efficient oxygen evolution electrocatalysis, Angew. Chem. Int. Ed. 56 (2017) 4502–4506.

[8] K.A. Stoerzinger, R.R. Rao, X.R. Wang, W.T. Hong, C.M. Rouleau, Y. Shao-Horn, The role of Ru redox in pH-dependent oxygen evolution on rutile ruthenium dioxide surfaces, Chem. 2 (2017) 668–675.

[9] R. Subbaraman, D. Tripkovic, K.C. Chang, D. Strmcnik, A.P. Paulikas, P. Hirunsit, M. Chan, J. Greeley, V. Stamenkovic, N.M. Markovic, Trends in activity for the water electrolyser reactions on 3d M(Ni,Co,Fe,Mn) hydr(oxy)oxide catalysts, Nat. Mater. 11 (2012) 550–557.

[10] M.S. Burke, S. Zou, L.J. Enman, J.E. Kellon, C.A. Gabor, E. Pledger, S.W. Boettcher, Revised oxygen evolution reaction activity trends for first-row transition-metal (oxy)hydroxides in alkaline media, J. Phys. Chem. Lett. 6 (2015) 3737–3742.

[11] C.G. Morales-Guio, L. Liardet, X. Hu, Oxidatively electrodeposited thin-film transition metal (oxy)hydroxides as oxygen evolution catalysts, J. Am. Chem. Soc. 138 (2016) 8946–8957.

[12] M. Xie, X. Xiong, L. Yang, X. Shi, A.M. Asiri, X. Sun, An $Fe(TCNQ)_2$ nanowire array on Fe foil: An efficient non-noble-metal catalyst for the oxygen evolution reaction in alkaline media, Chem. Commun. 54 (2018) 2300–2303.

[13] X. Ji, R. Zhang, X. Shi, A.M. Asiri, B. Zheng, X. Sun, Fabrication of hierarchical CoP nanosheet@microwire arrays: Via space-confined phosphidation toward high-efficiency water oxidation electrocatalysis under alkaline conditions, Nanoscale 10 (2018) 7941–7945.

[14] G.F. Chen, T.Y. Ma, Z.Q. Liu, N. Li, Y.Z. Su, K. Davey, S.Z. Qiao, Efficient and stable bifunctional electrocatalysts Ni/Ni_xM_y (M = P, S) for overall water splitting, Adv. Funct. Mater. 26 (2016) 3314–3323.

[15] W. Zhu, X. Yue, W. Zhang, S. Yu, Y. Zhang, J. Wang, J. Wang, Nickel sulfide microsphere film on Ni foam as an efficient bifunctional electrocatalyst for overall water splitting, Chem. Commun. 52 (2016) 1486–1489.

[16] J. Zhao, X. Li, G. Cui, X. Sun, Highly-active oxygen evolution electrocatalyzed by an Fe-doped $NiCr_2O_4$ nanoparticle film, Chem. Commun. 54 (2018) 5462–5465.

[17] M. Görlin, J.F. De Araujo, H. Schmies, D. Bernsmeier, S. Dresp, M. Gliech, Z. Jusys, P. Chernev, R. Kraehnert, H. Dau, P. Strasser, Tracking catalyst redox states and reaction dynamics in Ni-Fe oxyhydroxide oxygen evolution reaction electrocatalysts: The role of catalyst support and electrolyte pH, J. Am. Chem. Soc. 139 (2017) 2070–2082.

[18] R.D.L. Smith, C.P. Berlinguette, Accounting for the dynamic oxidative behavior of nickel anodes, J. Am. Chem. Soc. 138 (2016) 1561–1567.

[19] M. Ledendecker, S. Krick Calderón, C. Papp, H.-P. Steinrück, M. Antonietti, M. Shalom, The synthesis of nanostructured Ni_5P_4 films and their use as a non-noble bifunctional electrocatalyst for full water splitting, Angew. Chem. 127 (2015) 12538–12542.

[20] X. Yan, K. Li, L. Lyu, F. Song, J. He, D. Niu, L. Liu, X. Hu, X. Chen, From water oxidation to reduction: Transformation from $Ni_xCo_{3-x}O_4$ nanowires to $NiCo/NiCoO_x$ heterostructures, ACS Appl. Mater. Interfaces 8 (2016) 3208–3214.

[21] L. Kuai, J. Geng, C. Chen, E. Kan, Y. Liu, Q. Wang, B. Geng, A reliable aerosol-spray-assisted approach to produce and optimize amorphous metal oxide catalysts for electrochemical water splitting, Angew. Chem. Int. Ed. 53 (2014) 7547–7551.

[22] H.Y. Wang, Y.Y. Hsu, R. Chen, T.S. Chan, H.M. Chen, B. Liu, Ni^{3+}-induced formation of active NiOOH on the spinel Ni–Co oxide surface for efficient oxygen evolution reaction, Adv. Energy Mater. 5 (2015) 1–8.

[23] K. Xu, P. Chen, X. Li, Y. Tong, H. Ding, X. Wu, W. Chu, Z. Peng, C. Wu, Y. Xie, Metallic nickel nitride nanosheets realizing enhanced electrochemical water oxidation, J. Am. Chem. Soc. 137 (2015) 4119–4125.

[24] R. Xu, R. Wu, Y. Shi, J. Zhang, B. Zhang, Ni_3Se_2 nanoforest/Ni foam as a hydrophilic, metallic, and self-supported bifunctional electrocatalyst for both H_2 and O_2 generations, Nano Energy 24 (2016) 103–110.

[25] C. Tang, N. Cheng, Z. Pu, W. Xing, X. Sun, NiSe nanowire film supported on nickel foam: An efficient and stable 3D bifunctional electrode for full water splitting, Angew. Chem. Int. Ed. 54 (2015) 9351–9355.

[26] D.K. Bediako, Y. Surendranath, D.G. Nocera, Mechanistic studies of the oxygen evolution reaction mediated by a nickel-borate thin film electrocatalyst, J. Am. Chem. Soc. 135 (2013) 3662–3674.

[27] C. Xie, Y. Wang, D. Yan, L. Tao, S. Wang, In situ growth of cobalt@cobalt-borate core–shell nanosheets as highly-efficient electrocatalysts for oxygen evolution reaction in alkaline/neutral medium, Nanoscale 9 (2017) 16059–16065.

[28] J.M.V. Nsanzimana, V. Reddu, Y. Peng, Z. Huang, C. Wang, X. Wang, Ultrathin amorphous iron-nickel boride nanosheets for highly efficient electrocatalytic oxygen production, Chem. Eur. J. 24 (2018) 1–11.

[29] J.M.V. Nsanzimana, Y. Peng, Y.Y. Xu, L. Thia, C. Wang, B.Y. Xia, X. Wang, An efficient and earth-abundant oxygen-evolving electrocatalyst based on amorphous metal borides, Adv. Energy Mater. 8 (2018) 1–7.

[30] J. Masa, I. Sinev, H. Mistry, E. Ventosa, M. de la Mata, J. Arbiol, M. Muhler, B. Roldan Cuenya, W. Schuhmann, Ultrathin high surface area nickel boride (Ni_xB) nanosheets as highly efficient electrocatalyst for oxygen evolution, Adv. Energy Mater. 7 (2017) 1–8.

[31] K. Sun, F.H. Saadi, M.F. Lichterman, W.G. Hale, H.-P. Wang, X. Zhou, N.T. Plymale, S.T. Omelchenko, J.-H. He, K.M. Papadantonakis, B.S. Brunschwig, N.S. Lewis, Stable solar-driven oxidation of water by semiconducting photoanodes protected by transparent catalytic nickel oxide films, Proc. Natl. Acad. Sci. 112 (2015) 201423034.

[32] B.S. Yeo, A.T. Bell, In situ Raman study of nickel oxide and gold-supported nickel oxide catalysts for the electrochemical evolution of oxygen, J. Phys. Chem. C 116 (2012) 8394–8400.

[33] L. Trotochaud, S.L. Young, J.K. Ranney, S.W. Boettcher, Nickel-iron oxyhydroxide oxygen-evolution electrocatalysts: The role of intentional and incidental iron incorporation, J. Am. Chem. Soc. 136 (2014) 6744–6753.

[34] Y. Yang, H. Fei, G. Ruan, C. Xiang, J.M. Tour, Efficient electrocatalytic oxygen evolution on amorphous nickel-cobalt binary oxide nanoporous layers, ACS Nano 8 (2014) 9518–9523.

[35] X. Liu, M. Park, M.G. Kim, S. Gupta, G. Wu, J. Cho, Integrating NiCo alloys with their oxides as efficient bifunctional cathode catalysts for rechargeable zinc-air batteries, Angew. Chem. Int. Ed. 54 (2015) 9654–9658.

[36] X. Peng, L. Wang, L. Hu, Y. Li, B. Gao, H. Song, C. Huang, X. Zhang, J. Fu, K. Huo, P.K. Chu, In situ segregation of cobalt nanoparticles on VN nanosheets via nitriding of

$Co_2V_2O_7$ nanosheets as efficient oxygen evolution reaction electrocatalysts, Nano Energy 34 (2017) 1–7.

[37] J. Wu, Y. Xue, X. Yan, W. Yan, Q. Cheng, Y. Xie, Co_3O_4 nanocrystals on single-walled carbon nanotubes as a highly efficient oxygen-evolving catalyst, Nano Res. 5 (2012) 521–530.

[38] J. Wu, P. Guo, R. Mi, X. Liu, H. Zhang, J. Mei, H. Liu, W.-M. Lau, L.-M. Liu, Ultrathin $NiCo_2O_4$ nanosheets grown on three-dimensional interwoven nitrogen-doped carbon nanotubes as binder-free electrodes for high-performance supercapacitors, J. Mater. Chem. A 3 (2015) 15331–15338.

[39] Y. Zhao, S. Chen, B. Sun, D. Su, X. Huang, H. Liu, Y. Yan, K. Sun, G. Wang, Graphene-Co_3O_4 nanocomposite as electrocatalyst with high performance for oxygen evolution reaction, Sci. Rep. 5 (2015) 7629–7636.

[40] B.M. Hunter, J.D. Blakemore, M. Deimund, H.B. Gray, J.R. Winkler, A.M. Múller, Highly active mixed-metal nanosheet water oxidation catalysts made by pulsed-laser ablation in liquids, J. Am. Chem. Soc. 136 (2014) 13118–13121.

[41] Y. Wang, C. Xie, Z. Zhang, D. Liu, R. Chen, S. Wang, In situ exfoliated, N-doped, and edge-rich ultrathin layered double hydroxides nanosheets for oxygen evolution reaction, Adv. Funct. Mater. 28 (2018) 1703363.

[42] Y. Wang, Y. Zhang, Z. Liu, C. Xie, S. Feng, D. Liu, M. Shao, S. Wang, Layered double hydroxide nanosheets with multiple vacancies obtained by dry exfoliation as highly efficient oxygen evolution electrocatalysts, Angew. Chem. Int. Ed. 56 (2017) 5867–5871.

[43] T. Wang, Y. Guo, Z. Zhou, X. Chang, J. Zheng, X. Li, Ni-Mo Nanocatalysts on N-doped graphite nanotubes for highly efficient electrochemical hydrogen evolution in acid, ACS Nano 10 (2016) 10397–10403.

[44] J. Yin, Y. Li, F. Lv, Q. Fan, Y.-Q. Zhao, Q. Zhang, W. Wang, F. Cheng, P. Xi, S. Guo, NiO/CoN porous nanowires as efficient bifunctional catalysts for Zn − air batteries, ACS Nano 11 (2017) 2275–2283.

[45] L. Wang, C. Lin, D. Huang, F. Zhang, M. Wang, J. Jin, A comparative study of composition and morphology effect of $Ni_xCo_{1-x}(OH)_2$ on oxygen evolution/reduction reaction, ACS Appl. Mater. Interfaces 6 (2014) 10172–10180.

[46] S. Li, Y. Wang, S. Peng, L. Zhang, A.M. Al-Enizi, H. Zhang, X. Sun, G. Zheng, Co-Ni-based nanotubes/nanosheets as efficient water splitting electrocatalysts, Adv. Energy Mater. 6 (2016) 1–7.

[47] I. Abidat, C. Morais, C. Comminges, C. Canaff, J. Rousseau, N. Guignard, T.W. Napporn, A. Habrioux, K.B. Kokoh, Three dimensionally ordered mesoporous hydroxylated $Ni_xCo_{3-x}O_4$ spinels for the oxygen evolution reaction: On the hydroxyl-induced surface restructuring effect, J. Mater. Chem. A 5 (2017) 7173–7183.

[48] L. Trotochaud, J.K. Ranney, K.N. Williams, S.W. Boettcher, Solution-cast metal oxide thin film electrocatalysts for oxygen evolution, J. Am. Chem. Soc. 134 (2012) 17253–17261.

[49] M. Tahir, L. Pan, R. Zhang, Y.-C. Wang, G. Shen, I. Aslam, M.A. Qadeer, N. Mahmood, W. Xu, L. Wang, X. Zhang, J.-J. Zou, High-valence-state NiO/Co_3O_4 nanoparticles on nitrogen-doped carbon for oxygen evolution at low overpotential, ACS Energy Lett. 2 (2017) 2177–2182.

[50] W. Zhou, D. Kong, X. Jia, C. Ding, C. Cheng, G. Wen, $NiCo_2O_4$ nanosheet supported hierarchical core–shell arrays for high-performance supercapacitors, J. Mater. Chem. A 2 (2014) 6310.

[51] J. Bao, X. Zhang, B. Fan, J. Zhang, M. Zhou, W. Yang, X. Hu, H. Wang, B. Pan, Y. Xie, Ultrathin spinel-structured nanosheets rich in oxygen deficiencies for enhanced electrocatalytic water oxidation, Angew. Chem. Int. Ed. 54 (2015) 7399–7404.

[52] Z. Cai, Y. Bi, E. Hu, W. Liu, N. Dwarica, Y. Tian, X. Li, Y. Kuang, Y. Li, X.Q. Yang, H. Wang, X. Sun, Single-crystalline ultrathin Co_3O_4 nanosheets with massive vacancy defects for enhanced electrocatalysis, Adv. Energy Mater. 1701694 (2017) 1–8.

[53] L. Xu, Q. Jiang, Z. Xiao, X. Li, J. Huo, S. Wang, L. Dai, Plasma-engraved Co_3O_4 nanosheets with oxygen vacancies and high surface area for the oxygen evolution reaction, Angew. Chem. Int. Ed. 55 (2016) 5277–5281.

[54] C. Yuan, J. Li, L. Hou, X. Zhang, L. Shen, X.W. Lou, Ultrathin mesoporous $NiCo_2O_4$ nanosheets supported on Ni foam as advanced electrodes for supercapacitors, Adv. Funct. Mater. 22 (2012) 4592–4597.

[55] M.W. Louie, A.T. Bell, An investigation of thin-film Ni-Fe oxide catalysts for the electrochemical evolution of oxygen, J. Am. Chem. Soc. 135 (2013) 12329–12337.

[56] B.M. Jović, U. Lačnjevac, V.D. Jović, L.J. Gajić-Krstajić, J. Kovač, D. Poleti, N. V. Krstajić, Ni-(Ebonex-supported Ir) composite coatings as electrocatalysts for alkaline water electrolysis. Part II: Oxygen evolution, Int. J. Hydrogen Energy 41 (2016) 20502–20514.

[57] E.L. Ratcliff, J. Meyer, K.X. Steirer, A. Garcia, J.J. Berry, D.S. Ginley, D.C. Olson, A. Kahn, N.R. Armstrong, Evidence for near-surface NiOOH species in solution-processed NiO_x selective interlayer materials: Impact on energetics and the performance of polymer bulk heterojunction photovoltaics, Chem. Mater. 23 (2011) 4988–5000.

[58] X. Leng, Y. Shao, L. Wu, S. Wei, Z. Jiang, G. Wang, Q. Jiang, J. Lian, A unique porous architecture built by ultrathin wrinkled $NiCoO_2$/rGO/$NiCoO_2$ sandwich nanosheets for pseudocapacitance and Li ion storage, J. Mater. Chem. A 4 (2016) 10304–10313.

[59] Y. Chen, J. Hu, H. Diao, W. Luo, Y.F. Song, Facile preparation of ultrathin Co_3O_4/nanocarbon composites with greatly improved surface activity as a highly efficient oxygen evolution reaction catalyst, Chem. Eur. J. 23 (2017) 4010–4016.

[60] R. Kostecki, F. McLarnon, Electrochemical and in situ raman spectroscopic characterization of nickel hydroxide electrodes, J. Electrochem. Soc. 144 (1997) 485–493.

[61] S. Klaus, Y. Cai, M.W. Louie, L. Trotochaud, A.T. Bell, Effects of Fe electrolyte impurities on $Ni(OH)_2$/NiOOH structure and oxygen evolution activity, J. Phys. Chem. C 119 (2015) 7243–7254.

[62] J.R. Swierk, S. Klaus, L. Trotochaud, A.T. Bell, T.D. Tilley, Electrochemical study of the energetics of the oxygen evolution reaction at nickel iron (oxy)hydroxide catalysts, J. Phys. Chem. C 119 (2015) 19022–19029.

[63] M. Wehrens-Dijksma, P.H.L. Notten, Electrochemical quartz microbalance characterization of $Ni(OH)_2$-based thin film electrodes, Electrochim. Acta 51 (2006) 3609–3621.

[64] J. Keraudy, A. Ferrec, M. Richard-Plouet, J. Hamon, A. Goullet, P.Y. Jouan, Nitrogen doping on NiO by reactive magnetron sputtering: A new pathway to dynamically tune the optical and electrical properties, Appl. Surf. Sci. 409 (2017) 77–84.

Figure Captions

Scheme 1. Schematic illustration of the synthesis of NiCoON($NiCoO_2$/CoO/Ni_3N) on the NF.

Fig. 1. (a) Low-magnification SEM image and inset showing the high-magnification SEM image; (b) XRD pattern of NiCoON(1:2) NSAs/NF; (c) Low-magnification TEM and (d) High-resolution TEM image; (e) Ni 2p and (f) O 1s XPS spectra of $NiCo_2O_4$ (top) and NiCoON(1:2) NSAs/NF (bottom).

Fig. 2. (a) OER polarization curves (iR-compensated), (b) Tafel plots, and (c) Nyquist plots of the NF, $NiCo_2O_4$ NSAs/NF, and NiCoON(1:2) NSAs/NF in 1.0 M KOH; (d) Chronopotentiometric response of NiCoON(1:2) NSAs/NF at different current densities (10, 35, 55 mA cm^{-2}) in 1.0 M KOH for 30 h. The inset shows the iR-compensated polarization curves of NiCoON(1:2) NSAs/NF before and after 1,000 cycles of CV in 1.0 M KOH.

Fig. 3. (a) HR-TEM image of the post-OER NiCoON(1:2) nanosheet; (b) Ni 2p (upper) and O 1s (lower) XPS spectra of post-OER NiCoON(1:2) NSAs/NF; (c) Raman scattering spectra of pre- and post-OER NiCoON(1:2) NSAs/NF.

Fig. 4. (a) XRD patterns and (b) OER polarization curves of the samples (Ratio of Ni:Co is 1:2) which are annealed in NH_3 at various temperature. The inset in (b) shows the corresponding Tafel plots.

Fig. 5. (a) OER polarization curves (iR-compensated) of NiCoON NSAs/NF prepared with different Ni:Co ratios; (b) Tafel slopes and overpotentials required to reach j = 10 mA cm^{-2}

versus Ni:Co ratios; (c) Raman scattering spectra of NiCoON NSAs/NF for different Ni:Co ratios; (d) Intensity ratio of peaks i:ii in (c) as a function of Ni:Co ratios.

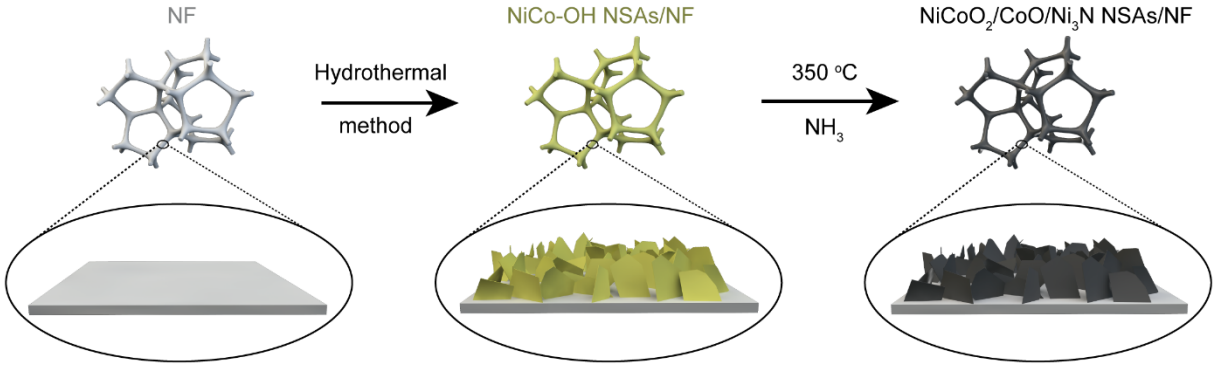
NF
Hydrothermal
method
NiCo-OH NSAs/NF
350 °C
NH3
NiCoO2/CoO/Ni3N NSAs/NF

Scheme 1.

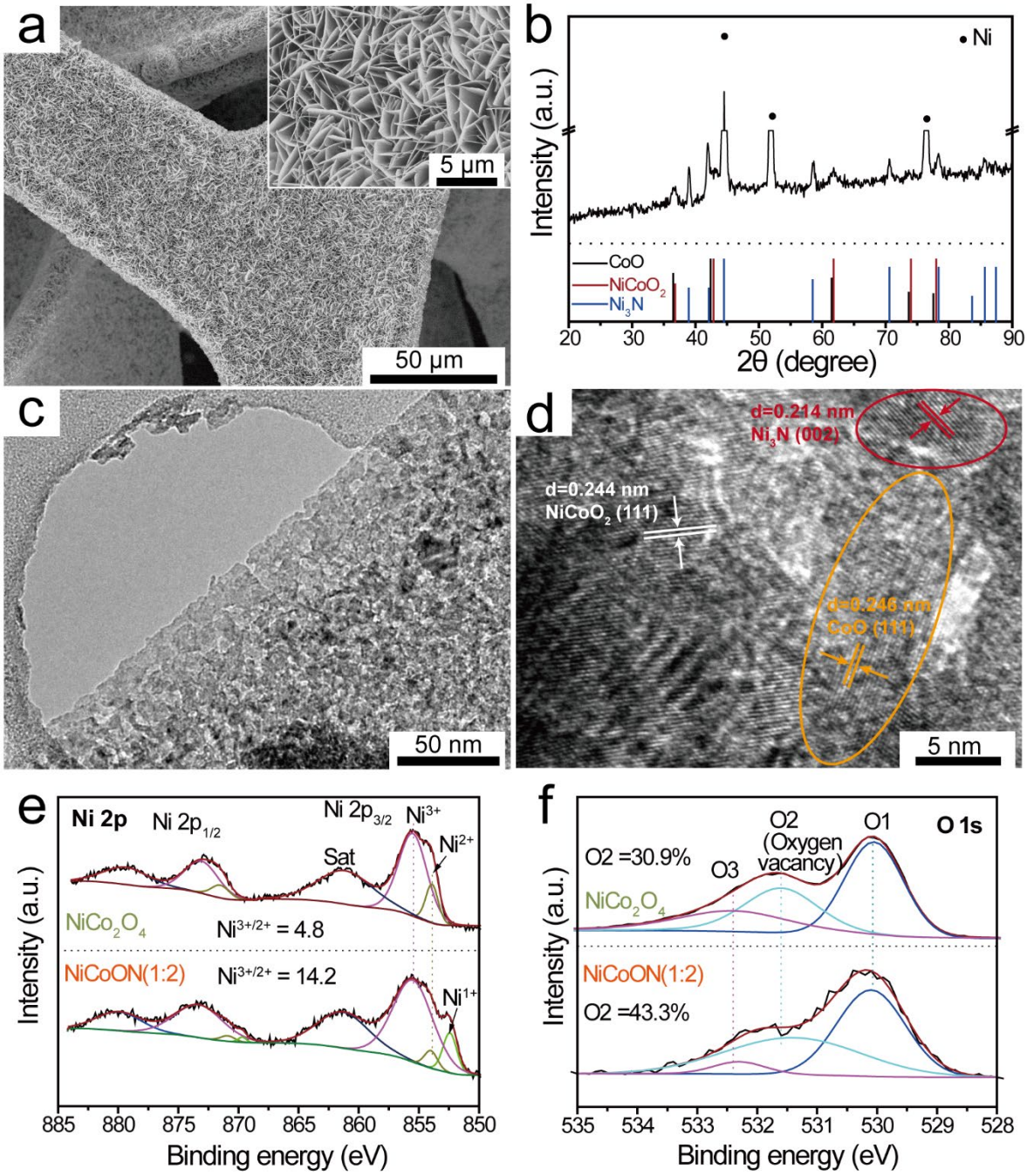
a
5 μm
50 μm
b
Ni
Intensity (a.u.)
CoO
NiCoO2
Ni3N
20 30 40 50 60 70 80 90
2θ (degree)
c
50 nm
d
d=0.214 nm
Ni3N (002)
d=0.244 nm
NiCoO2 (111)
d=0.246 nm
CoO (111)
5 nm
e
Ni 2p
Ni 2p1/2
Ni 2p3/2
Ni3+
Ni2+
Sat
NiCo2O4
Ni3+/2+ = 4.8
NiCoON(1:2)
Ni3+/2+ = 14.2
Ni1+
Intensity (a.u.)
885 880 875 870 865 860 855 850
Binding energy (eV)
f
O 1s
O2
(Oxygen
vacancy)
O1
O3
O2 =30.9%
NiCo2O4
NiCoON(1:2)
O2 =43.3%
Intensity (a.u.)
535 534 533 532 531 530 529 528
Binding energy (eV)

Figure 1.

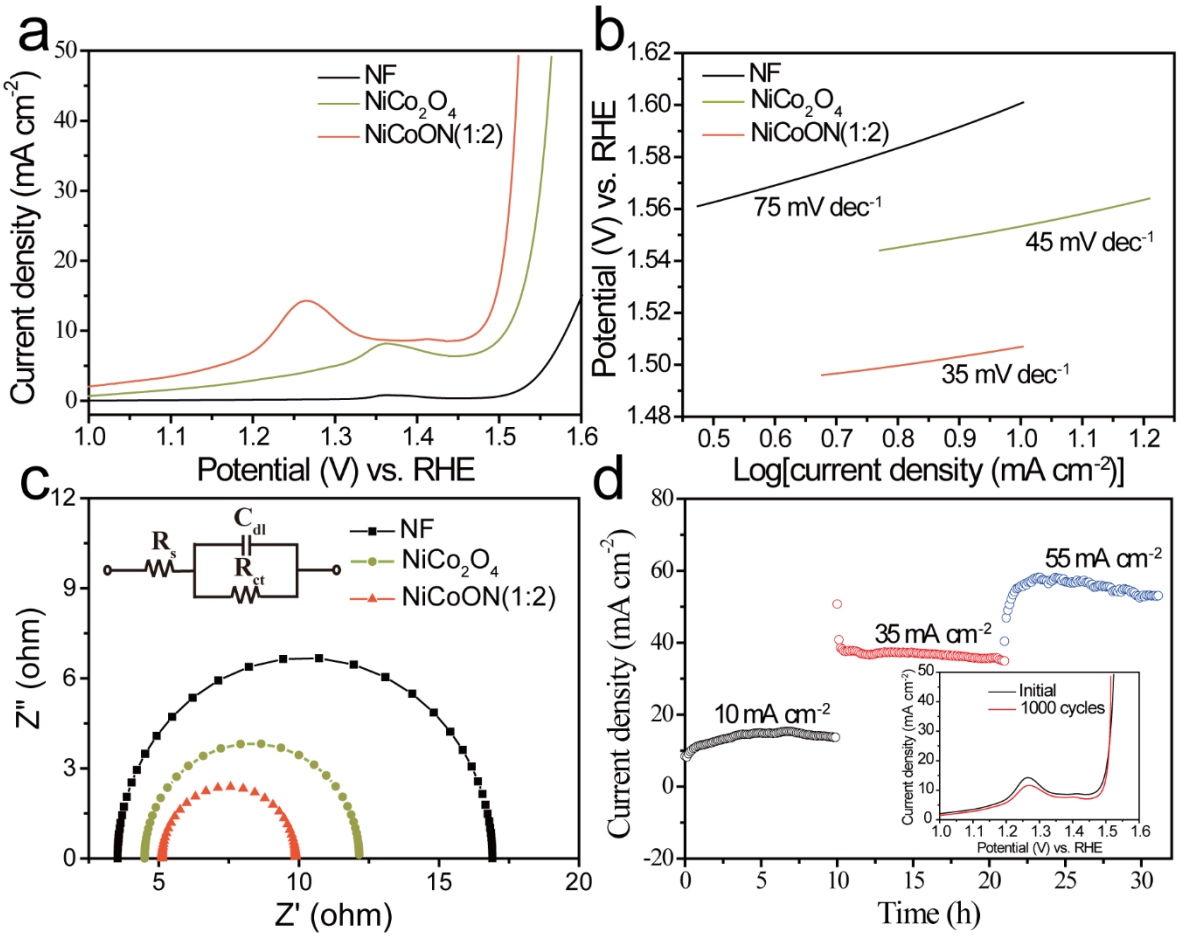
a
Current density (mA cm-2)
Potential (V) vs. RHE
NF
NiCo2O4
NiCoON(1:2)
b
Potential (V) vs. RHE
Log[current density (mA cm-2)]
75 mV dec-1
45 mV dec-1
35 mV dec-1
c
Z'' (ohm)
Z' (ohm)
Cdl
Rs
Rct
d
Current density (mA cm-2)
Time (h)
10 mA cm-2
35 mA cm-2
55 mA cm-2
Initial
1000 cycles

Figure 2.

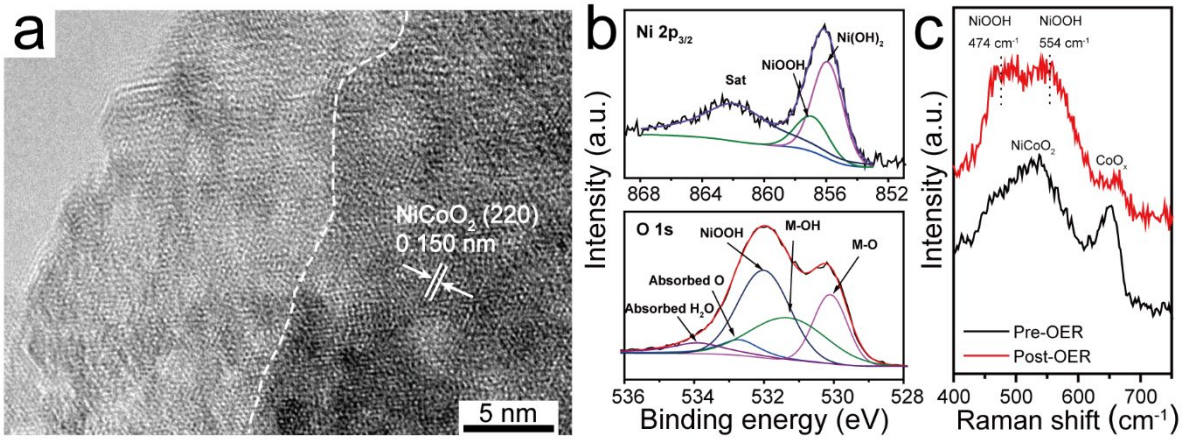
a
NiCoO2 (220)
0.150 nm
5 nm
b
Ni 2p3/2
Ni(OH)2
NiOOH
Sat
868
864
860
856
852
O 1s
NiOOH
M-OH
M-O
Absorbed O
Absorbed H2O
536
534
532
530
528
Binding energy (eV)
Intensity (a.u.)
c
NiOOH
474 cm-1
NiOOH
554 cm-1
NiCoO2
CoOx
Pre-OER
Post-OER
400
500
600
700
Raman shift (cm-1)
Intensity (a.u.)

Figure 3.

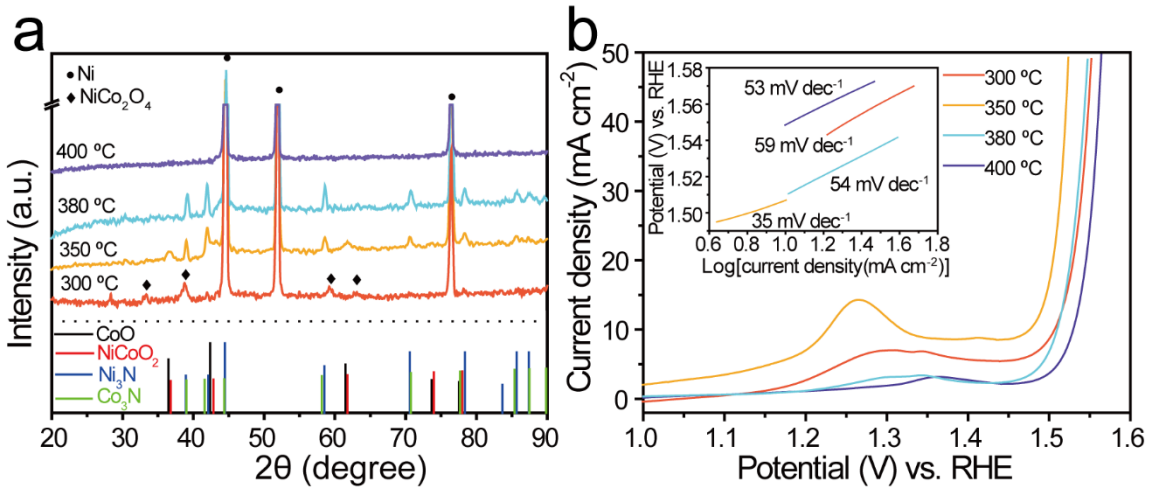
a
Ni
NiCo2O4
400 °C
380 °C
350 °C
300 °C
CoO
NiCoO2
Ni3N
Co3N
Intensity (a.u.)
20 30 40 50 60 70 80 90
2θ (degree)
b
Current density (mA cm-2)
0 10 20 30 40 50
1.0 1.1 1.2 1.3 1.4 1.5 1.6
Potential (V) vs. RHE
300 °C
350 °C
380 °C
400 °C
53 mV dec-1
59 mV dec-1
54 mV dec-1
35 mV dec-1
Potential (V) vs. RHE
1.50 1.52 1.54 1.56 1.58
0.6 0.8 1.0 1.2 1.4 1.6 1.8
Log[current density(mA cm-2)]

Figure 4.

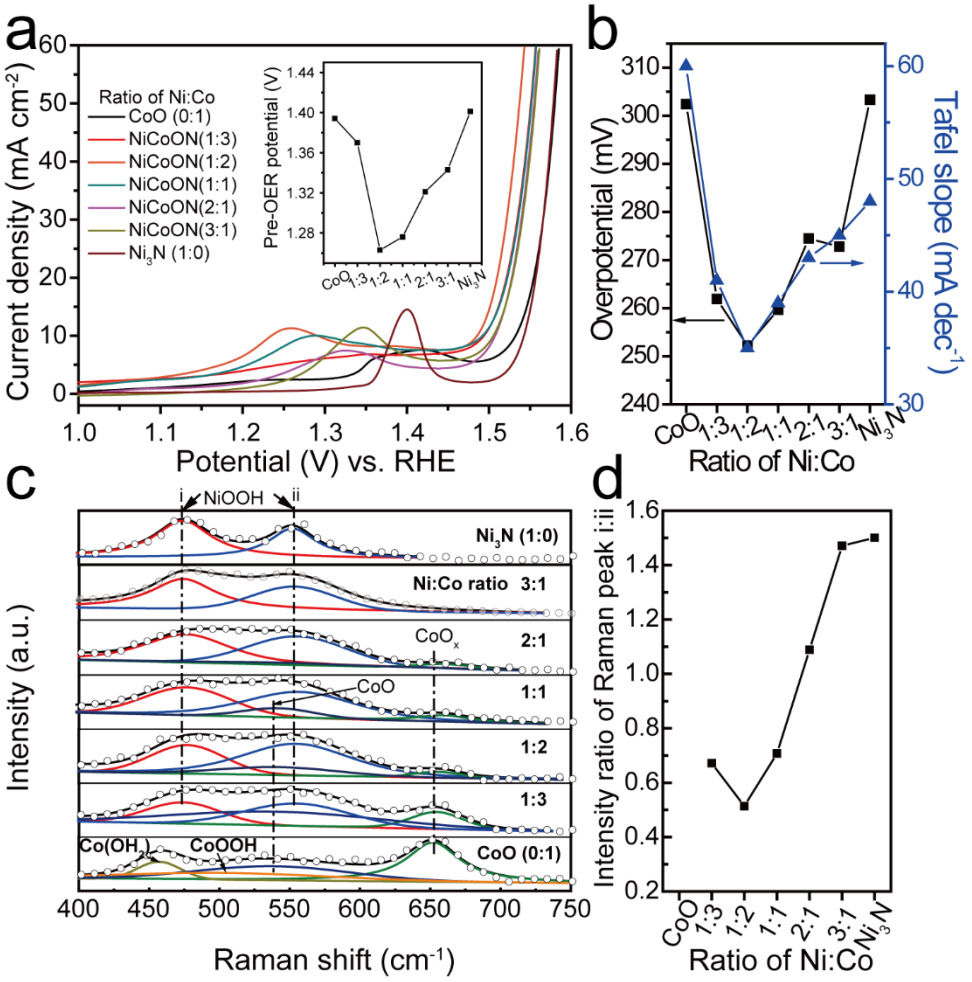
a
Current density (mA cm-2)
Potential (V) vs. RHE
Ratio of Ni:Co
CoO (0:1)
NiCoON(1:3)
NiCoON(1:2)
NiCoON(1:1)
NiCoON(2:1)
NiCoON(3:1)
Ni3N (1:0)
Pre-OER potential (V)
b
Overpotential (mV)
Tafel slope (mA dec-1)
Ratio of Ni:Co
c
NiOOH
i
ii
Ni3N (1:0)
Ni:Co ratio 3:1
CoOx
2:1
CoO
1:1
1:2
1:3
Co(OH)2
CoOOH
CoO (0:1)
Intensity (a.u.)
Raman shift (cm-1)
d
Intensity ratio of Raman peak i:ii
Ratio of Ni:Co

Figure 5.